Antenna Coupled MKID Performance Verification at 850 GHz for Large Format Astrophysics Arrays

Lorenza Ferrari, Ozan Yurduseven, *Student Member, IEEE*, Nuria Llombart, *Senior Member, IEEE*, Stephen J. C. Yates, Juan Bueno, Vignesh Murugesan, David J. Thoen, Akira Endo, Andrey M. Baryshev, and Jochem J. A. Baselmans

***Abstract*—Next generation sub-mm imaging instruments require kilo-pixel focal plane arrays filled with background limited detectors. Microwave kinetic inductance detectors (MKIDs) are a state-of-the-art detector for future instruments due to their inherent multiplexing capabilities. An MKID consists of a superconducting resonator coupled to a feed-line that is used for readout. In the device presented here radiation coupling is achieved by coupling the MKID directly to a planar antenna. The antenna is placed in the focus of an extended hemispherical lens to increase the filling factor and to match efficiently to fore optics. In this paper, we present the design and the optical performance of MKIDs optimized for operation in a 100-GHz band around 850 GHz. We have measured the coupling efficiency, frequency response, and beam patterns and compare those results to simulated performance. We obtain an excellent agreement between the measured and simulated beam pattern, frequency response, and absolute coupling efficiency between a thermal calibration source and the power absorbed in the detector. Additionally, we demonstrate that antenna coupled MKIDs offer background limited radiation detection down to ∼100 aW of power absorbed in the detector.**

***Index Terms*—Cryogenic, detectors, modeling, planar arrays, radiation pattern.**

I. Introduction

ASTRONOMICAL observations in the mm and sub-mm wavelength range (from 3 to 0.03 mm) probe the cold and distant universe. Young systems, either in early stage of star formation or high redshift galaxies, are embedded in dust which absorbs short-wavelength radiation and re-emits in the infrared region [1]. The study of these systems from the ground is performed at the telluric windows where the sky opacity is low. The Atacama Large Millimeter/submillimeter Array (ALMA) [2] is showing the potential of this approach unveiling new science every day. However, an interferometer like ALMA is effectively a single pixel instrument with a field of view identical to the beam size of a single telescope. Therefore, ALMA must be complemented by imaging systems with a large field of view in a narrow frequency band. Such imaging instruments require kilo-pixel arrays populated by sensors with the background limited sensitivity and high optical efficiency to maximize science output and on sky scanning speed and sensitivity. There are several proven technologies used in these frequency bands [3], [4]. However, later microwave kinetic inductance detectors (MKIDs) [5] are an excellent choice, due to their intrinsic multiplexing capability which makes reading-out large detector arrays relatively simple and cost effective. Instruments like MUSIC [6] or NIKA [7] and NIKA2 [8] are the pioneers in this field. Antenna coupled detectors have been largely employed in the past years due to the excellent performance [9]–[13]. In our case, the lens antenna consists of an extended hemispherical lens integrated with a double slot antenna, introduced first by [14] and developed further by [15]. The efficient radiation coupling between the twin slot antenna and the far field is achieved by means of a silicon lens as described in [16] and [17]. We choose this planar antenna because it is simple to design and fabricate and achieves good efficiency. The antenna is coupled to a distributed coplanar waveguide CPW line that connects the antenna to the MKID.

In this paper, we present in detail the pixel electromagnetic (EM) design, fabrication, and experimental evaluation of an antenna coupled niobium-titanium-nitride/aluminum (NbTiN-Al) hybrid MKID, optimized for radiation coupling in a small frequency band around 850 GHz. A similar experiment has been performed for the 350-GHz frequency band, as presented in [18], showing the versatility of our detector design. To design the MKID lens-antenna, we have developed a full EM model to optimize the antenna aperture efficiency for a given lens geometry and to match the frequency response. The model includes the superconductivity and finite thickness of the metal layers. For the lenses we used existing lenses, as a result the lens shape was not optimized. We measure the MKID beam patterns, frequency

Manuscript received April 11, 2017; revised August 20, 2017; accepted October 2, 2017. Date of publication November 28, 2017; date of current version January 9, 2018. This work was supported as part of a collaborative project, SPACEKIDs, funded via Grant 313320 provided by the European Commission under Theme SPA.2012.2.2-01 of Framework Programme 7. The work of N. Llombart was supported by ERC Starting under Grant ERC-2014-StG and under Grant LAA-THz-CC, 639749. The work of J. J. A. Baselmans was supported by the ERC COG 648135 MOSAIC. *(Corresponding author: Lorenza Ferrari.)*

L. Ferrari and S. J. C. Yates are with the SRON Netherlands Institute for Space Research, Groningen 9747AD, The Netherlands (e-mail: l.ferrari@sron.nl; s.yates@sron.nl).

O. Yurduseven, N. Llombart, and D. J. Thoen are with the Terahertz Sensing Group, Delft University of technology, Delft 2628CD, The Netherlands (e-mail: o.yurduseven@tudelft.nl; n.llombartjuan@tudelft.nl; d.j.thoen@tudelft.nl).

J. Bueno and V. Murugesan are with the SRON Netherlands Institute for Space Research, Utrecht 3584CA, The Netherlands (e-mail: j.bueno@sron.nl; v.murugesan@sron.nl).

A. Endo is with the Terahertz Sensing Group, Delft University of Technology, Delft 2628CD, The Netherlands (e-mail: a.endo@tudelft.nl).

A. M. Baryshev is with the Kapteyn Astronomical Institute, Groningen 9747AD, The Netherlands (e-mail: andrey@rug.nl).

J. J. A. Baselmans is with the SRON Netherlands Institute for Space Research, Utrecht 3584CA, The Netherlands, and also with the Terahertz Sensing Group, Delft University of Technology, Delft 2628CD, The Netherlands (e-mail: j.baselmans@sron.nl).

Color versions of one or more of the figures in this paper are available online at http://ieeexplore.ieee.org.

Digital Object Identifier 10.1109/TTHZ.2017.2764378

response, and radiation coupling efficiency and compare these to the EM model. We find that they to agree very well. This work builds upon previous results as described in [19] and [20] with the difference that: 1) we present here for the first time a full detailed design and experimental characterization and modeling of the MKID lens-antenna, and 2) in this paper the devices are fabricated on sapphire to ensure high yield. The experimental validation of the model demonstrates an end-to-end understanding of the detector physics and allows us to predict the expected performance of big arrays [21].

II. Device Design

MKIDs are superconducting pair-breaking detectors; therefore, the fundamental radiation absorption mechanism is the creation of quasi-particle excitations in a superconducting material [5]. The creation of quasi-particles changes the complex surface impedance of the superconductor, which is read-out by making the superconducting film part of a resonant circuit connected to a transmission line (called throughline in the remainder of the text). The change in surface impedance causes the resonance center frequency of the circuit to shift to lower values and the resonance dip depth to decrease. This effect can be readout by using a single tone close to the resonance frequency at the thermal equilibrium.

There are two main families of MKIDs: lumped element KIDs ("LEKIDs') [22] and lens-antenna coupled distributed MKIDs [23], [24]. The lumped element devices are easier to fabricate and assemble; the aluminum-based lens-antenna coupled devices are more flexible decoupling the KID optimization and the optical coupling allowing radiation coupling in principle at any wavelength from 3.3 mm (90 GHz) to 30 μm (10 THz) [25] by merely changing the antenna design. Around one mm wavelength aluminium LEKIDs and antenna coupled MKIDs have shown similar performance [7], [8], [18]. At higher frequencies antenna coupled devices are superior [21]. In addition, the high directional far field patterns of the lens-antenna allows for a higher temperature cold stop. Hence, the instrument thermal design and stray-light control become easier although at the cost of a more complex detector assembly. The distributed MKID consists of a shorted section of CPW line shunt-coupled to a CPW throughline. At the shorted end the CPW line also forms the feed of a twin slot antenna, which is coupled to the focus of a Si dielectric lens equipped with a $\lambda/4$ antireflection coating made from parylene-*C* [26].

The resonators have a wide and a narrow section (see Fig. 1): the wide region is introduced close to the coupler in order to reduce the two-level system noise [27]; the narrow section is connected to the feed of a twin slot antenna and made from NbTiN ground plane (GP) and an aluminum central line (2 μm wide and $\sim$1 mm long). NbTiN has a gap frequency of 1.1 THz, which allows creating a lossless circuit for both the readout frequency (4–8 GHz) as well as the radiation to be detected. On the contrary to the aluminum strip is resistive at 850 GHz frequency having a gap frequency of $\sim$90 GHz and, therefore, is capable of absorbing the radiation. The length of the strip is the result of an optimization between reduction of excess noise

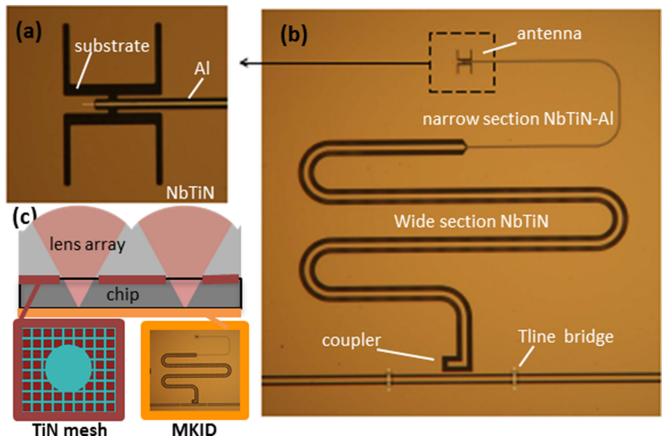

Fig. 1. (a) Antenna at the shorted end of the MKID resonator. (b) Photograph of a single MKID. To detect power in another frequency band only the antenna has to be different. The separate elements of the MKID are explicitly indicated. (c) Schematic diagram of the cross section of the assembled detector array with lens array, chip, and the position of the MKIDs and the TiN stray light absorbing mesh layer.

from the MKID and absorption efficiency. The design has two additional optimizations. One is the use of aluminum bridges to balance the throughline GPs at each side of the coupler, which prevent excess interpixel crosstalk [28]. The second optimization is introduced to absorb rescattered radiation and consists of a titanium-nitride (TiN) absorbing mesh located at the back side of the chip blocking radiation to transfer from one pixel to another [29].

III. Fabrication

The device is fabricated on a 350-μm-thick double side polished *C* plane sapphire wafer. The fabrication process includes the following steps. First, the reactive sputter deposition of a 5-nm Ti and 63-nm TiN bi-layer without vacuum break in, respectively, an argon (Ar) and argon-nitrogen (ArN) atmosphere from a Ti target. This deposition is done on the lens side of the wafer. Second is the deposition on the detector side of a 500-nm NbTiN layer using reactive magnetron sputtering in an argon-nitrogen plasma [30], [31] from an 81.9 wt.% Nb and 18.1wt.% Ti target. Patterning of the NbTiN resonator is done using contact lithography and a dry etch step using sulfurhexafluoride (SF_6) and oxygen to create a sloped edge on the thick NbTiN film, needed for a good contact to the last aluminum layer. Subsequently, we define the dielectric supports below the throughline bridges by spin-coating polymide, and subsequent baking and photolithography steps. A three-hour 250 °C cure under nitrogen atmosphere is done to make the polyimide stubs chemically resistant to further processing steps. In the next step, the wafer is soaked in a 10% HF solution for 10 s prior to the dc sputter deposition of a 40-nm-thick aluminum. The HF soak removes surface oxides and organic contaminations and guarantees a clean NbTiN-Al interface. Both NbTiN and TiN on the wafer backside are resistant against the HF etchant. The aluminum is wet etched to define the MKID hybrid sections and the throughline bridges. The last step is the patterning and etching

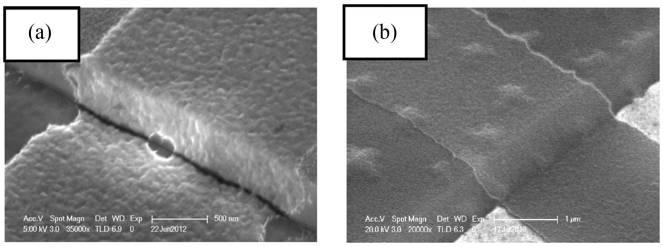

Fig. 2. (a) Micrograph photograph of the aluminum-NbTiN interface of a device fabricated on an all Si wafer. The Al is cut at the interface. (b) Micrograph photo of the aluminum-NbTiN interface fabricated on a sapphire substrate, the transition is smooth.

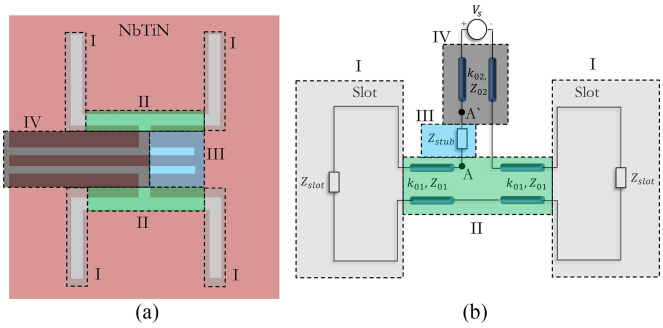

Fig. 3. (a) Double slot antenna integrated to a distributed CPW line attached together with a short-circuited stub, and (b) its RF equivalent circuit.

of the backside TiN layer in order to create the absorbing mesh, whereas the wafer front side is protected with photo resist.

The fabrication process is based upon *C* plane sapphire substrates instead of silicon because the Si process resulted in a limited device yield [32]. While processing on Si wafers, we have observed that the Al line is cut exactly at the edge of the NbTiN and Si interface (see Fig. 2). Our hypothesis of this problem is enhanced erosion of the aluminum at the Si-NbTiN interface due to the work function difference between the NbTiN and Si. Using an insulating substrate like sapphire prevents this process and has proven to create a very reliable process.

IV. Lens-Antenna EM Model

The lens antenna system has been designed using detailed computer simulation technology (CST) simulations [33]. Following the same approach, as described in [16] and [17], an analogue RF model of the double slot antenna can be derived. As sketched in Fig. 3, the RF model of the CPW fed antenna consists of four parts as follows:

1) the antenna slots (I);
2) a CPW line that connects the two slots (II);
3) a short-circuited stub attached to the center of the slot (III);
4) a distributed CPW transmission line that connects the antenna to the MKID (IV).

Starting from the classical design [15], the double slot geometry was optimized in terms of the quality of the radiated beams inside a semi-infinite dielectric as well as the antenna impedance

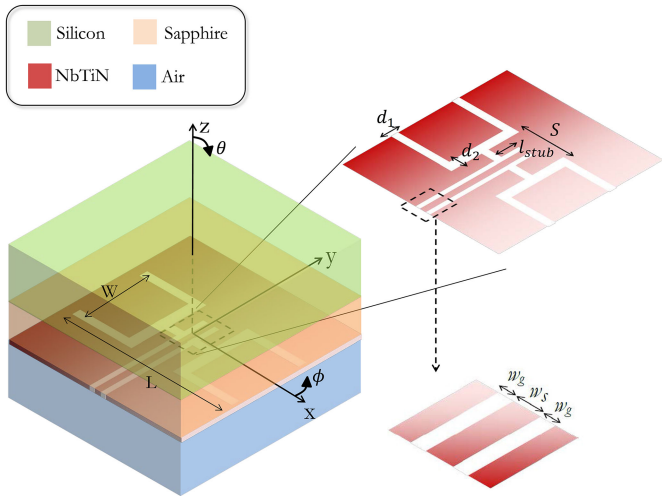

Fig. 4. Double slot geometry with its design parameters.

matching performance within the band of operation. The dielectric material stratification used for the antenna impedance optimization is highlighted in Fig. 4. A semi-infinite silicon dielectric ($\varepsilon_r = 11.9$) is located on top of an anisotropic *C* plane sapphire wafer with a thickness of 350 μm and $\varepsilon_r = 11.5$ parallel to the *C*-axis and $\varepsilon_r = 9.3$ perpendicular to the *C*-axis. With respect to previous double slot designs [15], [16], the connection to a distributed CPW line requires a larger separation *S,* which increases the cross polarization of the antenna. This separation was limited by the minimum feature size given by the fabrication. After the optimization of the beams, we focused on the optimization of the impedance match. In the current design, the slots are etched in a NbTiN GP with a kinetic inductance of 0.4 pH/sq and a finite thickness of 500 nm. In order to take the thickness and the kinetic inductance into account in the impedance optimization for the CST simulations, we took the following approach [33]: first, the effect of different materials properties for the GP was simulated assuming the GP is a two-dimensional (2-D) sheet. We use a perfect electric conductor (PEC) and NbTiN, which was modeled as a tabulated surface impedance in CST, with a characteristic kinetic inductance of 0.4 pH/sq, a value obtained from the dc resistivity ($100\,\mu\Omega \cdot$ cm), material thickness (500 nm) and critical temperature (15 K). Second, we evaluated the effect of the layer thickness using only a PEC GP, first in 2-D and then using the correct thickness of 500 nm. We used the simulation with a 2-D GP made of NbTiN as the design baseline and adjusted the design by treating the effect of the thickness as a multiplication factor to estimate the case of a superconductive GP with a 500-nm thickness.

Due to the anisotropy of the substrate and the kinetic inductance of the NbTiN GP, one needs to adjust the imaginary part of the impedance seen from the antenna input port. This problem was solved in the third step, by introducing a short circuited stub in series. This additional stub helps bringing the resonance frequency of the antenna to the desired value by means of adjusting the imaginary part of $Z_{\rm ant}$ accordingly. Finally, a distributed CPW line was attached to the double slot antenna geometry. The antenna is well matched within the band 750–910 GHz.

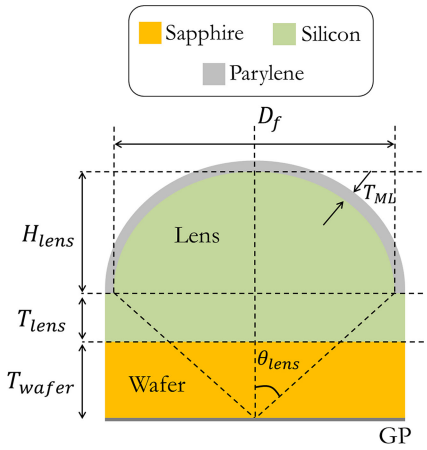

Fig. 5. Two- dimensional sketch of the lens geometry including the design parameters.

TABLE I
DESIGN PARAMETERS OF THE LENS GEOMETRY
(SEE FIG. 5 FOR THE DESIGN PARAMETERS)

Lens type	Elliptical
Wafer material	Sapphire ($\varepsilon_{x,y} = 9.3,\ \varepsilon_z = 11.5$)
Lens material	Silicon ($\varepsilon_r = 11.9$)
Matching layer	Parylene ML ($\varepsilon_r = 2.62$)
D_f	1.55 mm
$T_{\rm wafer}$	350 μm
$T_{\rm lens}$	200 μm
$H_{\rm lens}$	572 μm
$T_{\rm ML}$	54.5 μm
$\theta_{\rm lens}$	55°

TABLE II
DESIGN PARAMETERS OF THE DOUBLE SLOT ANTENNA

L	98.82 μm
W	56.47 μm
d_1	3 μm
d_2	6 μm
S	12 μm
w_g	2 μm
w_s	2 μm
$l_{\rm stub}$	8.75 μm

Once the twin slot antenna design was fixed, we integrated the design to an existing silicon lens with the geometrical parameters highlighted in the CST model shown in Fig. 5.

Tables I and II report explicitly the design parameters of the double slot antenna and the lens design, respectively. In the CST simulations, we use the first transmitted pulse to eliminate the additional field contributions due to the internal reflections inside the single lens. The lens is coated by a $\lambda_d/4 = 55$ μm Parylene *C* matching layer (ML) with $\mathrm{n} = 1.62$. Here, λ_d is the wavelength in the dielectric at the center frequency and an absorbing material is used to evaluate the power trapped in the dielectric. From this simulation, we can derive the efficiencies described in Appendix A. Fig. 6 and Table III give the most important efficiency terms contributing to the optical coupling efficiency, $\eta_{\rm op}(v) = \eta_{\rm rad}(\nu)\eta_{\rm SO}(\nu)$ for our experiment.

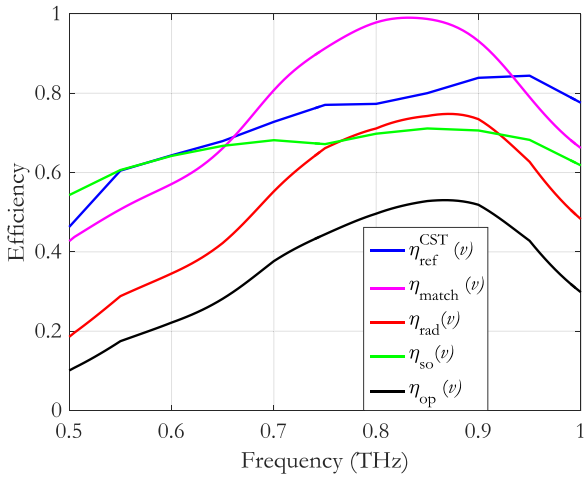

Fig. 6. Efficiency calculations obtained from the optimized double slot fed lens antenna.

TABLE III
CALCULATED EFFICIENCIES OF THE LENS-ANTENNA @850 GHz

Aperture efficiency	Optical coupling efficiency
$\eta_{\rm rad} = 0.74$	$\eta_{\rm rad} = 0.74$
$\eta_{\rm tap} = 0.78$	$\eta_{\rm SO} = 0.71$
$\boldsymbol{\eta}_{\rm ap} = 0.58$	$\boldsymbol{\eta}_{\rm op} = 0.53$

The radiation efficiency $\eta_{\rm rad}$ is the product of three terms as follows.

1) $\eta_{\rm ref}^{\rm CST}(\nu)$ evaluates how much power remains in the dielectric. In the present lens geometry, this value is limited to 80% at the central frequency due to the fixed solid angle to the lens (55°), losing about 13% more power compared to a wider angle lens.
2) $\eta_{\rm match}$ gives the match between the MKID CPW and the antenna, $\eta_{\rm match}(\nu) > 90\%$, within 750–910-GHz band.
3) $\eta_{\rm CPW}$, which has been estimated to be about 94% using [33], is the term associated to the radiation losses in the CPW line.

The spill-over efficiency $\eta_{\rm SO}(\nu)$ is calculated for a solid angle of $\Omega_s = \pm 14.3°$ (to be compared to the experiment) using the fields radiated by the lens antenna. The maximum optical coupling efficiency is 53% and it is observed at the designed frequency, 850 GHz. Table III explicitly reports the antenna efficiencies at the centre frequency of 850 GHz, including the antenna taper efficiency $\eta_{\rm tap}$ and aperture efficiency $\eta_{\rm ap}$ as well. The value of the aperture efficiency is smaller than the reported 78% in [15], due to the factors described above [for example $\eta_{\rm ref}^{\rm CST}(\nu)$], plus a 10% lower taper efficiency due to the anisotropy of the sapphire wafer.

V. MEASUREMENTS AND RESULTS

We have fabricated a detector chip with 4 MKIDs in a linear configuration, the array has a single pixel exactly on the chip center and, therefore, in the optical axis of the experimental systems. The MKIDs on this chip are all identical, except the

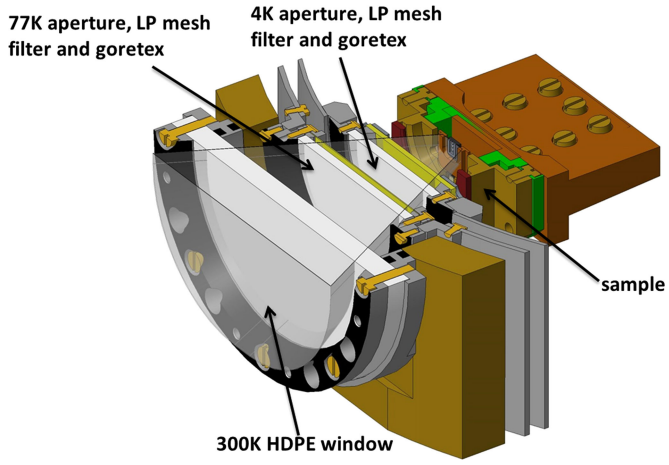

Fig. 7. Cross section of the He3 cryostat. From the right to the left they are drawn: the sample, 4-K shield, 77-K shield and 300-K window.

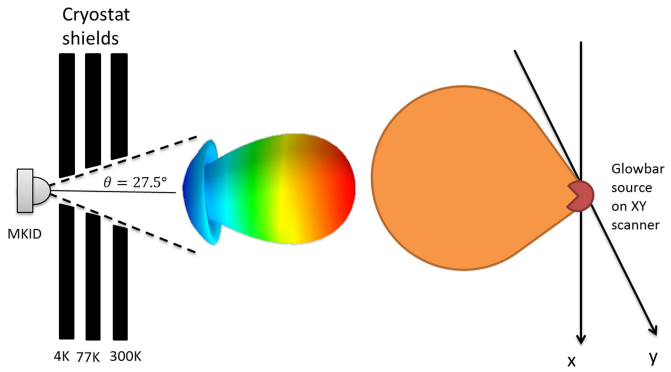

Fig. 8. Schematic diagram of the beam pattern setup. The cryostat optical access is defined by apertures, goretex/HDPE and metal mesh filters. The radiation patterns are measured by scanning a glowbar source mounted on a *XY* scanner, in an image plane.

length of the resonator allowing us to read each pixel at a different readout frequency. After fabrication, the chip is mounted in a sample holder, and the lens array is glued to the chip using a dedicated alignment tool and cyanoacrylate glue. Below, we discuss the experimental setup to measure the antenna beam pattern, frequency response, and the device sensitivity and optical efficiency. Note that in all experiments, we use the so-called MKID phase response. This is motivated by the fact that MKID phase readout gives the largest dynamic range, and importantly, allows for the multiplexing of much more pixels [34]. This is not needed in the present small chip experiment, but crucial for the actual use of these devices, as shown for example in [21]. Additionally, we use the frequency sweep to convert the MKID complex response to a frequency response. This removes to first-order nonlinearity of the MKID phase response, which originates from the limited bandwidth of the resonance [35].

A. Beam Patterns

The antenna frequency response and beam maps require direct access from the chips to the 300-K lab environment, hence we use a dedicated cryogenic test facility optimized for these measurements. The sample is mounted on the cold stage of a ^{3}He sorption cooler, which is mounted on the cold plate of a wet ^{4}He 4.2 K cryostat equipped with a liquid nitrogen cooled shield at 77 K. The ^{3}He stage temperature is 290 mK under nominal operation and the hold time is longer than 8 h. The optical access consists of a 300K HDPE window, Goretex infrared blockers, and metal mesh low-pass filters at 77 K and 4 K. The apertures on the 77-K and 4-K stages limit the total angular throughput of the radiation to an opening angle of $\pm 27.5°$. The absence of fore optics ensures direct access to the lens antenna system. The cryostat optical access has been designed with particular care in order to prevent reflections by using absorbing coatings on all surfaces. The coating is made from EPOTEK 920 epoxy mixed with 3% by weight carbon black powder in which are embedded 1-mm rms diameter grains of SiC grains [36] (see Fig. 7).

The beam patterns are measured by scanning a 2-mm-diameter hot source in 2 directions in the plane perpendicular to the optical axis of the cryostat (see Fig. 8). The hot source is made from a Newport IR source in the focus of an elliptical mirror assembly; a 2-mm-diameter aperture is located in the second focus of the elliptical mirrors in order to create theoretically a uniform illumination as a function of angle. The area around the hot source aperture is coated with radiation absorber to prevent standing waves. Additionally in order to remove drifts, we introduce an optical chopping mechanism located behind the source aperture. The hot source is chopped at $\sim$80 Hz, modulating above the system 1/f noise dominated by thermal and background loading drifts. Linearization using to effective KID resonant frequency using the scheme outlined in [35] removes the associated changes in responsivity to the $\sim$10% level across the beam pattern. Also, we measure the response of each pixel as a function of the source position simultaneously by using our multitoned readout system [34]. By positioning a polarizer in front of the source a specific polarization direction can be probed.

The measured and simulated beam patterns in copole (performed with the polarizer) agree very well (see Figs. 9 and 10). There are uncertainties in the measurements due to detector noise (off-main beam noise floor), beam truncation, and misalignment of the limiting aperture, for example due to thermal contraction. Additional effects can come from the finite sized grid, back reflections into the cryostat modifying the thermal background, and slightly asymmetric beam of the hot source. The compression of the beam in the *E* plane is attributed to these setup uncertainties. The *E* plane cut, perpendicular to the slots, and the *H* plane cut, parallel to the slots, are different due to the effect of the sapphire birefringence.

For the measurements of the cross-pole response of the detector, we mount a polarizing wire grid in front of the hot source aperture to prevent beam truncation. This arrangement required particular care of reflections from the environment back to the cryostat. In addition, the grid available for the measurements is measured to have a leakage of the order of –18 dB. This is clearly visible in the beam patterns measured. To compensate,

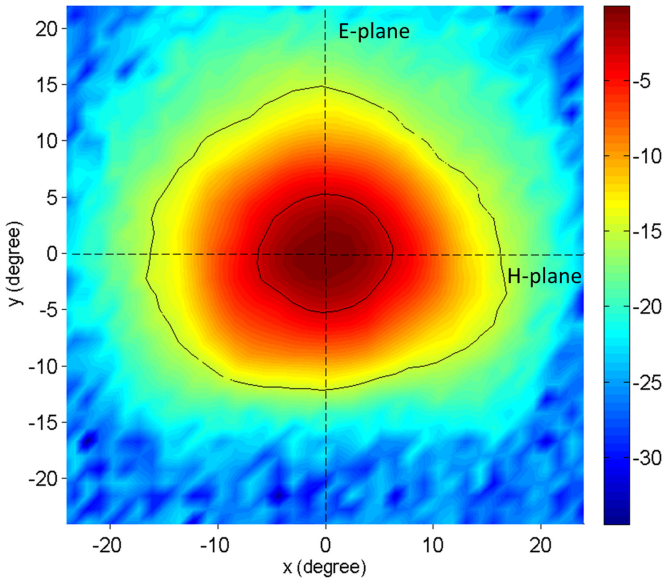

Fig. 9. Two-dimensional beam pattern of the lens antenna system in the far field. The contours level are located at –3 dB and –15 dB. The cutting planes used for Fig. 10 are also shown. The center of the beam pattern is found by a Gaussian fit of the beam shape. The scale is in dB.

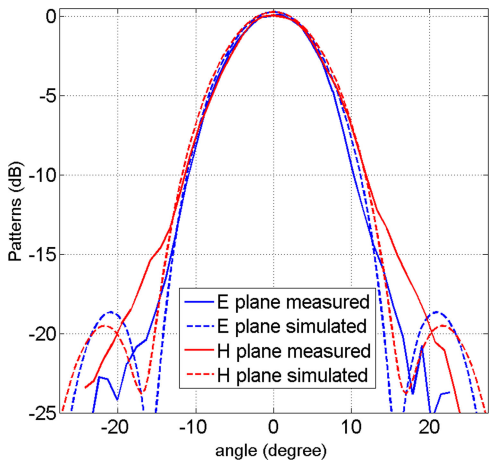

Fig. 10. Measured and simulated beam pattern for one pixel of the device. The *E* plane corresponds to a cross section perpendicular to the antenna slots; vice versa the *H* plane is the cross section parallel to the slots. The simulations are single frequency (850 GHz) while the measurements are wide band.

we introduce a postprocessing analysis where we subtract the co-pol beam pattern from the raw cross-pole measurement in order to get the expected null at the center of the cross-pole beam pattern.

The agreement between calculations and experiment is reasonable (see Figs. 11 and 12). We do observe the asymmetry in the clover but the patterns are broader and one lobe is suppressed, the reason is unclear but we attribute this effect to setup uncertainties as indicated for the copol measurement, in addition the KID resonator can contribute to the cross-pol emission (this contribution is not included in our CST model).

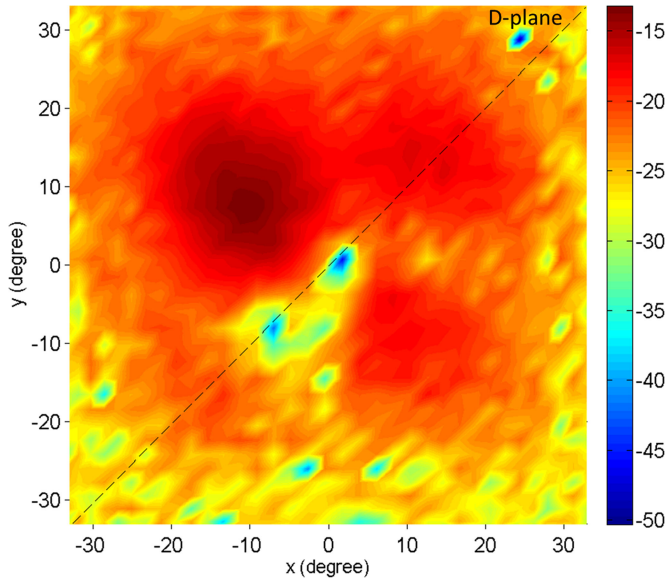

Fig. 11. Two-dimensional cross-polarization beam pattern of the lens antenna system in the farfield. The scale is in dB. The maximum is normalized to the maximum value of the copolarization beam pattern, and for better visualization the color scale is varied.

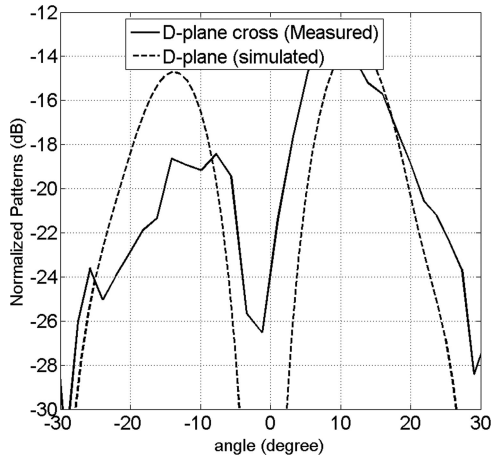

Fig. 12. Cross pol beam pattern, corresponding to the *D* plane located 45° between the *E* plane and *H* plane. The simulations are single frequency (850 GHz) while the measurements are wide band.

B. Antenna Frequency Response

The lens-antenna frequency response is measured by means of a Fourier transform spectrometer (FTS) in a classical Michelson interferometer setup. Referring to the scheme showed in Fig. 8, the FTS replaces the *XY* scanner.

The FTS consists of a glowbar source at 1600 K, a fixed mirror and a movable mirror and a mylar beamsplitter. The MKIDs are the detectors in this setup and their phase responses were measured as a function of the mirror distance. The beam is stopped down with an aperture to a solid angle of roughly 14°, a similar value used for simulations in order to be able to compare the two results. The phase response is linear in power, as verified using a rotating polarizer in another experiment. The Fourier transform of the interferogram is corrected for the

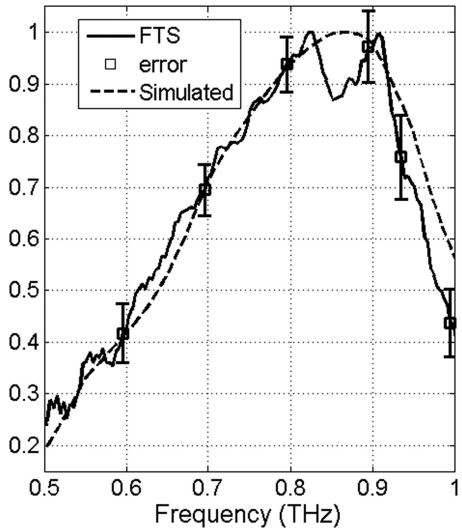

Fig. 13. Simulated and measured antenna FTS (in a.u.) versus frequency.

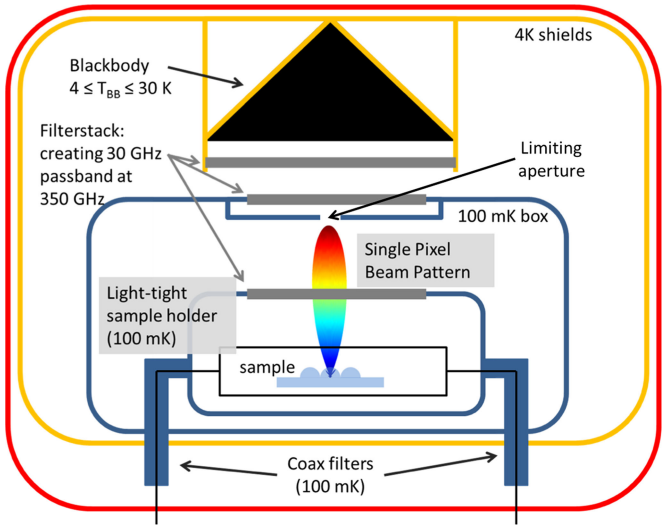

Fig. 14. Schematic representation to measure the optical efficiency of a direct detector, image taken with permission from [19].

frequency dependency of the filters and beamsplitters. The errors are given by the uncertainty in the beamsplitter thickness and the filters transmission.

Fig. 13 compares the simulated with the measured FTS response. The agreement between the measurements data and the model is excellent.

C. Optical Efficiency and Sensitivity

The sensitivity measurements are performed in an adiabatic demagnetization refrigerator (ADR) cryostat with an operating temperature of 120 mK. The cryostat is equipped with a thermal calibration source, as depicted in Fig. 14 and explained in [19] and [37], where we can control with high accuracy the throughput, power and frequency of sub-mm radiation falling on the detector. The detector chip is mounted inside a light-tight sample holder, which itself is mounted inside a light-tight box. Both are thermally anchored to the 120-mK stage of the ADR cooler and well shielded against stray radiation [36]. Above the light-tight box a blackbody radiator is mounted, consisting of a copper cone coated on its inside with radiation absorber/emitter consisting of a mixture of 1-mm SiC grains and Epotek epoxy with 3% by weight carbon black. The blackbody is weakly coupled to its surrounding shield, which is thermally anchored to the 3K stage of the cooler. Resistive heaters and a PID control allow us to control the blackbody temperature $(T_{\rm BB})$ between 3 and 40 K and thereby the power emitted. Quasi-optical filters are mounted on the radiator enclosure, light-tight box, and sample holder to define the frequency band of the radiation admitted to the sample holder. The aperture in the outer 120-mK light-tight box determines the throughput, in the experiment considered it is a 10.2 mm diameter aperture at 20-mm distance, i.e., the half opening angle is 14.3°. Using this geometry and the calculated and measured detector beam pattern we find $\eta_{\rm SO} = 0.71$.

The measurements strategy of the detector's optical efficiency and sensitivity is described in detail in Appendix B. In Figs. 15 and 16, we give the results of the experiment. The center panel of Fig. 15 shows the phase noise power spectral density $S_\theta(f)$, obtained at nine different blackbody temperatures, i.e., nine different values of P_s. We clearly observe a white noise spectrum and a power dependent roll off. For the curves, where the roll off changes with blackbody temperature, we are sure that the device is background limited [19], this is the case for the five highest values of P_s. Importantly, the noise level at frequencies below the roll off (indicated by the vertical line) is much higher than the noise floor of the system, visible at the highest frequencies, i.e., -113 dBc/Hz.

This implies that we can neglect any intrinsic detector noise in the remainder of the analysis. Subsequently, we measure the MKID Phase response $d\theta/dP_s$ around each blackbody temperature. This is done by a linear fit to the MKID phase response to a change in blackbody temperature, converted into a dP_s using (B.4). The result is shown in the top panel of Fig. 15. Now all parameters in (B.6) are known and as a result we can obtain $\eta_{\rm op}$, for measurements at the five highest powers, because only for those we know that the detector reaches background limited performance. The result is shown in Fig. 16. The optical efficiency is 0.58 ± 0.05. The error is obtained from the propagation of the error in the noise equivalent power (NEP) (noise and fit errors) and combining the error in the mean value of the data points and the mean of the errors of all points. This agrees within the errors with the calculated value $\eta_{\rm op} = 0.53$.

Since now both $\eta_{\rm op}$ and $\eta_{\rm SO}$ are experimentally validated, the latter by the good agreement between measured and calculated beam pattern, we can confirm that the calculated values of $\eta_{\rm rad}$ and $\eta_{\rm ap}$ are an accurate description of the performance of the detector. The bottom panel of Fig. 15 shows the measured experimental NEP and background limited $\rm NEP_{BLIP}$, calculated using (B.1) as function of $P_{\rm abs}$, using $\eta_{\rm op} = 0.58$. It is clear that for the five highest powers we find an excellent agreement as expected. For the lowest powers the MKID is no longer background limited, but limited by thermal fluctuations in the device. As a result the NEP no longer decreases with power and saturates, as observed in [37]. So, we conclude that the device can be described by $\rm NEP_{Blip}(P_{abs})$ for $P_{\rm abs} > 5$ fW.

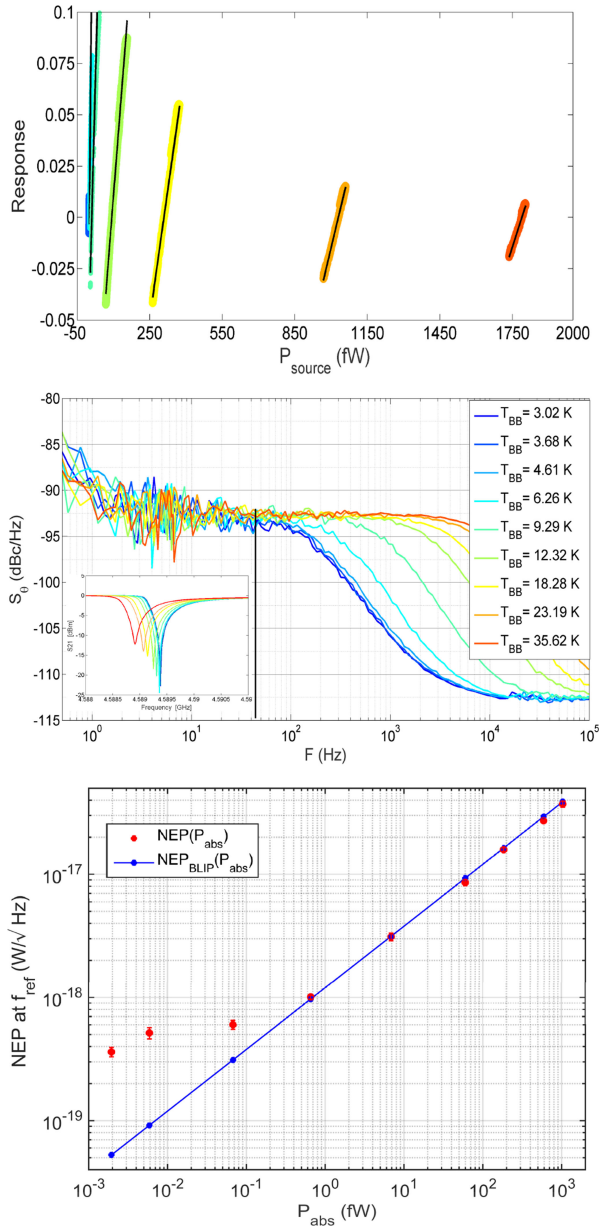

Fig. 15. TOP: MKID phase response to a small change in source power around several center values of Ps. We also show the linear fits to this response used to calculate the NEP CENTER: Phase noise power spectral density for several values of T_{BB}. Note the white spectrum and the increase in the roll-off frequency with increasing T_{BB}, proving that the device is background limited. BOTTOM: $\mathrm{NEP}_{\mathrm{BLIP}}(P_{\mathrm{abs}})$ and $\mathrm{NEP}(P_{\mathrm{abs}})$, i.e., as a function the power absorbed in the aluminum of the MKID. The system has a measured coupling efficiency $\eta_{\mathrm{op}} = 0.58$ between calibration source and detector, i.e., the system NEP is $\sim 1/\sqrt{\eta_{\mathrm{op}}}$ worse than the data presented. The aperture efficiency of the detector is $\eta_{\mathrm{ap}} = 0.65$. Above ~ 5 fW both $\mathrm{NEP}_{\mathrm{Blip}}(P_{\mathrm{abs}})$ and $\mathrm{NEP}(P_{\mathrm{abs}})$ are identical, proving that the detector reaches full background limited performance above that value, and that the optical efficiency obtained is correct. All values are obtained at a frequency F = 70 Hz, which can be seen to be in the white region of the noise spectra in the top panel.

VI. Conclusion

We have shown that we have reached a full understanding and characterization of the EM properties of the antenna coupled NbTiN-Al kinetic inductance detectors as indicated by the good agreement between experimental measurements and theoretical simulations. We have designed, fabricated, and experimentally characterized an MKID device optimized for detection of the atmospheric window centered at 850 GHz. The device shows background limited performance with a coupling efficiency $\eta_{\mathrm{op}} = 0.58$ and an aperture efficiency $\eta_{\mathrm{ap}} = 0.58$ at absorbed power levels in excess of 5 fW. At lower powers the sensitivity saturates at a $\mathrm{NEP} = 3.5 \cdot 10^{-19}\,\mathrm{W}/\sqrt{\mathrm{Hz}}$. Furthermore, we find excellent agreement between the EM model predicting the antenna beam pattern, frequency response, and coupling efficiency.

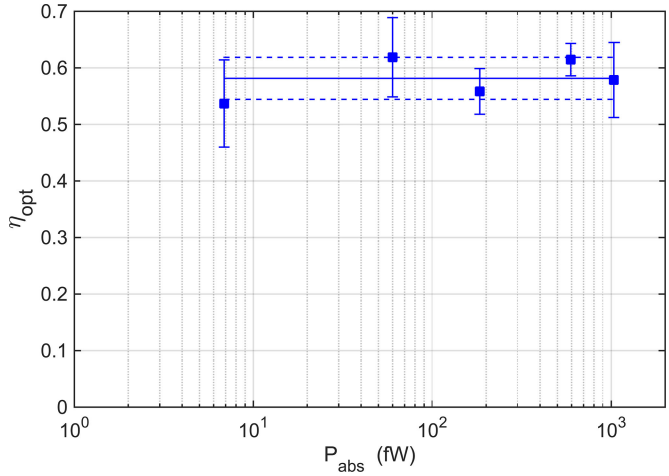

Fig. 16. Optical efficiency for each black-body temperature. We use the five highest powers to obtain the average value of 0.58. The data points at lower blackbody temperatures are not fully background limited, and can therefore not be used in this analysis. The lines are indicating the 1s error.

Appendix A
Power Absorbed by a Lens-Antenna Coupled MKID

In this appendix, we describe how to evaluate the power received by a MKID coupled to a lens antenna from an incoherent source with an average temperature T distributed over a solid angle of Ω_s (Fig. A.1 gives a graphical representation of the considered configuration).

The power absorbed by a detector in the presence of a blackbody can be described using the Planck's curve as

$$P_{\mathrm{abs}} = \frac{1}{2}\int\int_{\Omega_s} B_s(\nu)\, A_{\mathrm{eff}}^{\mathrm{tel}}(\nu,\Omega)\, F(\nu)\, d\Omega d\nu \qquad \text{(A.1)}$$

where $B_s(\nu) = \frac{f^2}{c^2}\frac{2hf}{e^{\frac{hf}{k_B T}}-1}$ is the source brightness, A_{eff} is the detector effective area, the factor $\frac{1}{2}$ is associated to a single-polarized antenna, and $F(\nu)$ is the filter frequency response.

For single-mode antenna coupled detectors, the effective area can be expressed as function of the antenna physical area A_{lens}, aperture efficiency η_{ap}, and antenna normalized radiation pattern $P(\nu,\Omega)$

$$A_{\mathrm{eff}}^{\mathrm{tel}}(\nu,\Omega) = A_{\mathrm{lens}}\eta_{\mathrm{ap}}(\nu)\, P(\nu,\Omega) \qquad \text{(A.2)}$$

where the normalized radiation pattern can be expressed as function of the antenna directivity pattern $P(\nu,\Omega) = D(\nu,\Omega)/D(\nu,0)$. One can express the aperture efficiency as the product of the radiation efficiency $\eta_{\mathrm{rad}}(\nu)$ and the taper efficiency $\eta_{\mathrm{tap}}(\nu)$. For directive antennas, the taper efficiency

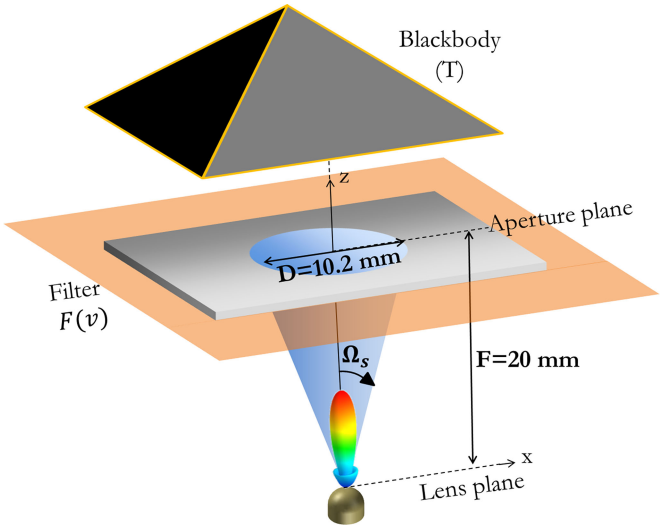

Fig. A.1. Lens-antenna coupled MKID in presence of an incoherent source.

relates the broadside directivity to the maximum directivity that one could achieved for the lens area

$$\eta_{\mathrm{tap}}(\nu) = \frac{D(\nu,0)}{4\pi A_{\mathrm{lens}}}\lambda^2. \tag{A.3}$$

Therefore, (A.1) becomes

$$P_{\mathrm{abs}} = \frac{1}{2}\int B_s(\nu)\,\lambda^2 F(\nu)\,\eta_{\mathrm{rad}}(\nu)\,\frac{1}{4\pi}\int_{\Omega_s} D(\nu,\Omega)\,d\Omega d\nu. \tag{A.4}$$

The angular integral can be expressed as a spill over efficiency term $\eta_{\mathrm{so}}^{\Omega_s}(\nu)$ by using the definition of the directivity $D(\nu,0) = \frac{4\pi}{\int_{4\pi} P(\nu,\Omega)d\Omega}$

$$P_{\mathrm{abs}} = \frac{1}{2}\int B_s(\nu)\,\lambda^2 F(\nu)\,\eta_{\mathrm{rad}}(\nu)\,\eta_{\mathrm{so}}^{\Omega_s}(\nu)\,d\nu. \tag{A.5}$$

With $\eta_{\mathrm{so}}^{\Omega_s}(\nu) = \frac{\int_{\Omega_s} P(\nu,\Omega)d\Omega}{\int_{4\pi} P(\nu,\Omega)d\Omega}$. The product $\eta_{\mathrm{rad}}(\nu)\eta_{so}^{\Omega_s}(\nu)$ will be referred here as the optical coupling efficiency $\eta_{op}(\nu)$.

Whereas the spill over term in the optical coupling efficiency depends basically on the radiation pattern of the lens antenna, the radiation efficiency represents the fraction of the power that is absorbed by the central conductor of the CPW line in the MKID. This efficiency term can be evaluated simulating the antenna in transmission (input port at the antenna feed point) using the CST model shown in Fig. 6. The radiation efficiency divided into the following contributions.

- $\eta_{\mathrm{ref}}^{\mathrm{CST}}$ fractional radiated power after the lens with respect to the power accepted by the antenna port in CST simulation. This efficiency quantifies the power trapped inside the dielectric.
- η_{match} the impedance matching efficiency between the antenna feed and the MKID CPW line impedance.
- η_{CPW} the efficiency associated on how much power is absorbed by the central conductor of the MKID CPW [36].

When a filter is used in the measurements with relative bandwidth much smaller than that of the antenna, as seen in Fig. B.1 for the present case, the optical efficiency can be taken out from the spectral integral in (A.5)

$$P_{\mathrm{abs}} \approx \frac{1}{2}\eta_{\mathrm{op}}(\nu_0)\int B_s(\nu)\,\lambda^2 F(\nu)\,d\nu. \tag{A.6}$$

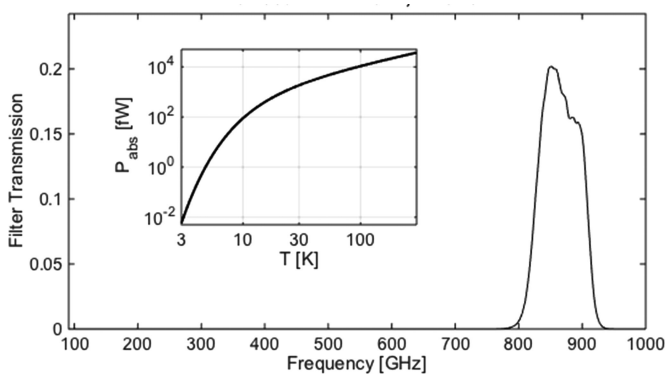

Fig. B.1. Transmission of all filters in the experimental setup, the peak transmission is 0.2, note that the out of band rejection is better than –60 dB between 80 GHz and 10 THz. The insert shows P_{abs} as a function of blackbody temperature.

Appendix B
Absolute Measurement of the Detector Coupling

As explained in Appendix A the lens-antenna coupled MKID is a single mode detector. The maximum throughput is λ^2 and the power absorbed in the MKID depends both on the detector beam and on the aperture size to the thermal radiator. As a consequence, we need two independent experiments to measure the aperture efficiency η_{ap} of a lens-antenna coupled MKID: 1) a measurement of the lens-antenna beam pattern and 2) a measurement of the optical coupling efficiency between a thermal calibration source and the detector [19].

A. Measurement of the Beam Pattern to Determine η_{tap}

To measure the beam pattern the MKID is placed in a cryostat with optical access to the lab, and the response as a function of the position of a well-calibrated source is measured as explained in detail in the paper. Due to limits in cooling power we can only measure the pattern inside a cone with a limited opening angle of $\pm 27.5°$, and we compare this measurement with the simulated patterns. If the experimental patterns match the calculated pattern, we can use the simulated beam pattern, available over the whole sphere to calculate η_{SO} and η_{tap}. We obtain $\eta_{\mathrm{tap}} = 0.78$ for the 850-GHz lens antenna. Note that 90% of the detector throughput is included in the measurement, so we have to rely on the calculation only for a very limited amount of total power.

B. Measurement of η_{op} to determine η_{rad}

A thermal radiator introduces a noise to the signal due to the quantized nature of the photons emitted. A detector is called background limited if its sensitivity is given only by the intrinsic signal to noise of the source. In this limit, the NEP of the MKID per unit of bandwidth is given by [39][1]

$$\mathrm{NEP}_{\mathrm{Blip}}^2 = \mathrm{NEP}_{\mathrm{Poisson}}^2 + \mathrm{NEP}_{\mathrm{wave}}^2 + \mathrm{NEP}_R^2$$

[1]The last term in [B.1] has a prefactor 4, in [5], [22], and [23] a prefactor of 2 is used. The results in the paper are only affected a bit by this difference.

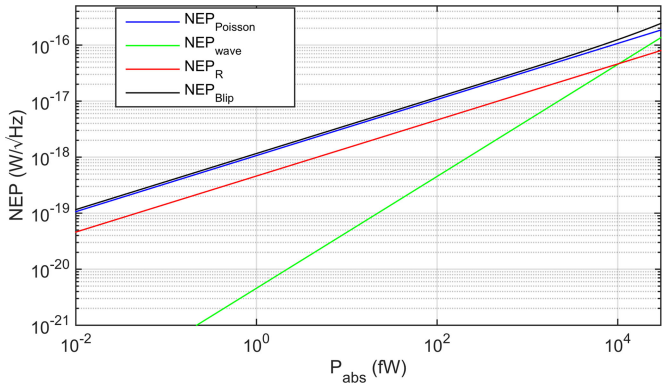

Fig. B.2. Background limited NEP and its contributions as a function of $P_{\rm abs}$ for our experiment.

which can be evaluated for the case of a narrow band-pass filter around a center frequency ν_0 [40], [41]

$$\mathrm{NEP}^2_{\mathrm{Blip},\nu 0} = \int \left(2P_\nu h\nu + 2P_\nu h\nu m O_\nu + 4\Delta P_\nu/\eta_{pb}\right) d\nu \tag{B.1}$$

with

$$P_\nu \approx \frac{1}{2}\eta_{\rm op}\left(\nu_0\right) B_s\left(\nu\right)\lambda^2 F\left(\nu\right)$$

i.e., $P_{\rm abs} = \int P_\nu {\rm d}\nu$. In this equation ${\rm m} = \eta_{\rm op}\cdot {\rm F}(\nu)$ is the total efficiency of photon absorption between the blackbody calibrator and the aluminum of the MKID and $O_\nu = \left(e^{\frac{h f}{k_B T}} - 1\right)^{-1}$ is the occupation per mode. In our setup, F(ν) is maximum in the filter passband for F(ν)$\sim$0.18 between 830 and 890 GHz (see Fig. B.1) and $\eta_{\rm op} = 0.58$, with the result that m$\sim$0.1. Furthermore, η_{pb} is the efficiency of creating a quasi-particle, which for our aluminum film is approximately 0.4 at frequencies above 180 GHz, but increasing to 1 at 90 GHz [37]. Below 90 GHz aluminum does not absorb radiation.

The first term in (B.1) is the Poisson noise due to random photon fluctuations. This term dominates in the Wien limit (hν>kT) where photon arrival events are completely random and can be described by Poisson statistics. Hence, in this limit $\mathrm{NEP}_{Blip,\nu 0} \approx \mathrm{NEP}_{\rm Poisson} = (2P_{\rm abs}{\rm h}\nu_0)^{1/2}$. The second term is the wave bunching term, which dominates in the Raileigh-Jeans limit (hν<kT) providing that *m* is not too small. In this limit, $\mathrm{NEP}_{Blip,\nu 0} \approx \mathrm{NEP}_{\rm wave} \propto {\rm k}T d\nu$, i.e., independent of frequency. The last term in (B.1) is the noise added due to random recombination of quasi-particles in the MKID. This term deteriorates the NEP for an MKID slightly compared to for example a TES detector. In our experiment, the total NEP is increased by 9% due recombination noise. In Fig. B.2, we show all NEP contributions. Note that the bunching or wave contribution starts to become important for power levels far exceeding the experiment described in the main text.

Experimentally, we can obtain the NEP of a MKID by measuring the noise power spectral density $S_x(f)$ at a constant blackbody temperature and by measuring the device response to a small variation absorbed power $dx/dP_{\rm abs}$

$$\mathrm{NEP}\left(P_{\rm abs}, f\right) = \sqrt{S_x\left(f\right)}\left(\frac{dx}{dP_{\rm abs}}\right)^{-1}\sqrt{1+\left(2\pi f\tau_{\rm qp}\right)}\,. \tag{B.2}$$

Here the parameter *x* is the MKID observable, commonly the MKID phase response θ or MKID amplitude response, and $\tau_{\rm qp}$ is the quasi-particle lifetime, $\tau_{\rm qp} \propto P_{\rm abs}^{-1/2}$ and of the order of 1 ms for aluminum MKIDs under dark conditions [37]. The parameter f denotes the frequency information of the power spectral density, typically between 0.1 Hz and 1 MHz. Since S_x has a white spectrum under background limited conditions the NEP is independent of frequency for frequencies $f_{\rm ref} < \left(2\pi\tau_{\rm qp}\right)^{-1} \sim 70$ Hz. To allow a direct comparison to (B.1) we obtain the experimental NEP at $f_{\rm ref}$, typically around 60 Hz to limit effects of 1/*f* noise using

$$\mathrm{NEP}_{\rm exp}\left(P_{\rm abs}, f_{\rm ref}\right) = \sqrt{S_x\left(f_{\rm ref}\right)}\left(\frac{dx}{dP_{\rm abs}}\right)^{-1}. \tag{B.3}$$

If $\eta_{\rm op}$ is known (B.1) allows us to calculate the background limited NEP and (B.3) allows us to obtain the experimental NEP from the measured data.

If we want to experimentally determine $\eta_{\rm op}$, we need to start from known quantities. We calculate the power emitted per unit of bandwidth from the blackbody in a single mode multiplied with the transmission of our quasi-optical filters $P_{s,\nu}$

$$P_{s,\nu} \approx \frac{1}{2}B_s\left(\nu\right)\lambda^2 F\left(\nu\right) \tag{B.4}$$

i.e., $P_\nu = \eta_{\rm op}\cdot P_{s,\nu}$. Hence, the total blackbody power transmitted through the filters that can coupled to a single mode is given by $P_s = \int P_{s,\nu}\, d\nu$. These definitions allow us to rewrite (B.1) and (B.3) into

$$\mathrm{NEP}^2_{\mathrm{Blip},\nu 0} = \ldots.$$
$$\int \left(2\eta_{\rm op}P_{s,\nu}h\nu + 2\eta_{\rm op}^2 P_{s,\nu}h\nu F\left(\nu\right)BO_\nu + \frac{4\Delta\eta_{\rm op}P_{s,\nu}}{\eta_{pb}}\right) d\nu$$
$$\mathrm{NEP}^2_{\rm exp} = \eta_{\rm op}^2 S_x\left(f_{\rm ref}\right)\left(\frac{dx}{dP_s}\right)^{-2} \tag{B.5}$$

respectively. Since for a background limited MKID $\mathrm{NEP}_{\rm exp} \triangleq \mathrm{NEP}_{\mathrm{BLIP},\nu 0}$, we can obtain the optical efficiency

$$\eta_{\rm op} = \frac{\int 2P_{s,\nu}h\nu\delta\nu + \int 4\Delta\eta_{\rm op}P_{s,\nu}/\eta_{\rm pq}\delta\nu}{\mathrm{NEP}^2_{\rm exp} - \int 2P_{s,\nu}h\nu F_\nu O_\nu\delta\nu} \tag{B.6}$$

which is valid for a narrow frequency band around ν_0. The experimental measurement of $\eta_{\rm op}$ can be combined with a calculation of $\eta_{\rm SO}$ which is based on the calculated, and experimentally validated beam pattern, to obtain the radiation efficiency $\eta_{\rm rad}(\nu_0) = \eta_{\rm op}(\nu_0)/\eta_{\rm SO}(\nu_0)$.

ACKNOWLEDGMENT

The authors would like to thank M. Eggens, R. van der Schuur, and J. Panman for the technical support and availability and also T. Klapwijk for useful discussions.

REFERENCES

[1] D. Scott *et al.*, "The submillimeter universe," White Paper, Canadian 2010, Long Range Planning process, 2010, arXiv:1008.4159.

[2] ALMA. [Online]. Availbale: www.almaobservatory.org

[3] W. S. Holland *et al.*, "SCUBA-2: The 10 000 pixel bolometer camera on the James Clerk Maxwell telescope," *Monthly Notices Roy. Astron. Soc.*, vol. 430, no. 4, pp. 2513–2533, 2013.

[4] V. Reveret *et al.*, "The ArTéMiS wide-field submillimeter camera: Preliminary on-sky performances at 350 microns," in *Proc. SPIE Conf.*, Jun. 2014, p. 5, doi:10.1117/12.2055985.

[5] P. K. Day, H. G. Leduc, B. A. Mazin, A. Vayonokis, and J. Zmuidzinas, "A broadband superconducting detector suitable for large arrays," *Nature*, vol. 425, pp. 817–821, 2003.

[6] J. Sclaerth *et al.*, "A millimeter and sumillimeter kinetic inductance detector camera," *J. Low Temp. Phys.*, vol. 151, no. 3/4, pp. 684–689, 2008.

[7] A. Monfardini *et al.*, "NIKA: A millimeter-wave kinetic inductance camera," *Astron. Astrophys.*, vol. 521, 2010, Paper A29.

[8] M. Calvo *et al.*, "The NIKA2 instrument, A dual-band kilopixel KID array for millimetric astronomy," *J. Low Temp. Phys.*, vol. 184, pp. 816–823, 2016.

[9] M. M. Gitin, F. W. Wise, G. Arijavalingam, Y. Pastol, and R. C. Compton, "Broad-band characterization of millimeter-wave log-periodic antennas by photoconductive sampling," *IEEE Trans. Antennas Propag.*, vol. 42, no. 3, pp. 335–339, Mar. 1994.

[10] A. Semenov, H. Richter, B. Gunther, H-W. Huebers, and J. Karamarkovic, "Integrated planar log spiral antenna at terahertz waves," in *Proc. IEEE Int. Workshop Antenna Technol. Small Antennas Novel Metamaterials*, 2005, pp. 197–200.

[11] A. D. Semenov *et al.*, "TeraHertz performance of integrated lens antennas with a hot-electron bolometer," *IEEE Trans. Microw. Theory Techn.*, vol. 55, no. 2, pp. 239–247, Feb. 2007.

[12] B. S. Karasik and R. Cantor, "Demonstration of high optical sensitivity in far-infrared hot-electron bolometer," *Appl. Phys. Lett.*, vol. 98, 2011, Art. no. 193503.

[13] S. Cherednichenko, V. Drakinskiy, T. Berg, P. Khosropanah, and E. Kollberg, "Hot-electron bolometer terahertz mixers for the herschel space observatory," *Rev. Sci. Instrum.*, vol. 879, 2008, Art. no. 034501.

[14] J. Zmuidzinas and H. G. Leduc, "Quasi-optical slot antenna SIS mixer," *IEEE Trans. Microw. Theory Tech.*, vol. 41, no. 10, pp. 1797–1804, Sep. 1992.

[15] D. Filipovic, S. Gearhart, and G. Rebeiz, "Double-slot antennas on extended hemispherical and elliptical silicon dielectric lenses," *IEEE Trans. Microw. Theory Techn.*, vol. 41, no. 10, pp. 1738–1749, Oct. 1993.

[16] P. Focardi, R. M. Williams, and A. Neto, "Design guidelines for terahertz mixers and detectors," *IEEE Trans. Microw. Theory Techn.*, vol. 53, no. 5, pp. 1653–1661, May 2005.

[17] P. Focardi, A. Neto, and W. R. McGrath, "Coplanar-waveguide-based terahertz hot electron-bolometer mixers-improved embedding circuit description," *IEEE Trans. Microw. Theory Techn.*, vol. 5, no. 10, pp. 2374–2383, Oct. 2002.

[18] L. Ferrari *et al.*, "Performance verification of a double slot antenna with an elliptical lens for large format KID arrays," *Proc. SPIE*, vol. 9914, Jun. 2016, Art. no. 99142G, doi: 10.1117/12.2235315.

[19] R. M. J. Janssen *et al.*, "High optical efficiency and photon noise limited sensitivity of microwave kinetic inductance detectors using phase readout," *Appl. Phys. Lett.*, vol. 103, 2013, Art. no. 203503.

[20] R. M. J. Janssen *et al.*, "Performance of hybrid NbTiN-Al microwave kinetic inductance detectors as direct detectors for sub-millimeter astronomy," in *Proc. SPIE*, vol. 9153, Aug. 2014, doi: 10.1117/12.2055537.

[21] J. J. A. Baselmans *et al.*, "A kilo-pixel imaging system for future space based far-infrared observatories using microwave kinetic inductance detectors," *Astron. Astrophys.*, vol. 601, 2017, Art. no. 29653.

[22] S. Doyle, P. Mauskopf, J. Naylon, A. Porch, and C. Duncombe, "Lumped element kinetic inductance detectors," *J. Low Temp. Phys.*, vol. 151, pp. 530–536, 2008.

[23] P. K. Day *et al.*, "Nuclear Instruments and Methods in Physics Research Section A: Accelerators, Spectrometers, Detectors and Associated Equipment," in *Proc. Int. Workshop Low Temp. Detectors*, vol. 559, pp. 329–860, 2006.

[24] H. McCarrick *et al.*, "Horn-coupled, commercially-fabricated aluminum lumped-element kinetic inductance detectors for millimeter wavelengths," *Review Scientific Instruments*, vol. 85, 2014, Art. no. 123117.

[25] J. Bueno *et al.*, "Full characterisation of a background limited antenna coupled KID over an octave of bandwidth for THz radiation," *Appl. Phys. Lett.*, vol. 110, 2017, Art. no. 233503, doi: 10.1063/1.4985060.

[26] M. Ji, C. Musante, S. Yngvesson, A. J. Gatesman, and J. Waldman, "Study of Parylene as anti-reflection coating for silicon optics at THz frequencies," in *Proc. 11th Int. Symp. Space Terahertz Technol.*, Ann Arbor, MI, USA, 2000, p. 398.

[27] J. Gao *et al.*, "A semiempirical model for two-level system noise in superconducting microresonators," *Appl. Phys. Lett.*, vol. 92, 2008, Art. no. 212504.

[28] S. J. C. Yates, J. J. A. Baselmans, A. M. Baryshev, and L. Ferrari, "Clean beam patterns with low crosstalk using 850 GHz microwave kinetic inductance detectors," *J. Low Temp. Phys.*, vol. 176, pp. 761–766, 2014.

[29] S. J. C. Yates, "Surface wave control for large arrays of microwave kinetic inductance detectors," *IEEE Trans. THz Sci. Technol.*, vol. 7, no. 6, pp. 789–799, Nov. 2017.

[30] B. G. C. Bos *et al.*, "Reactive magnetron sputter deposition of superconducting Niobium Titanium Nitride thin films with differernt target sizes," *IEEE Trans. Appl. Supercond.*, vol. 27, no. 4, Jun. 2017, Art. no. 1500405.

[31] D. J. Thoen *et al.*, "Superconducting NbTiN thin films with highly uniform properties over a 100 mm wafer," *IEEE Trans. Appl. Supercond.*, vol. 24, no. 4, Jun. 2017, Art. no. 1500505.

[32] K. Cheng, "Effects of ohmic metal on electrochemical etching of GaAs in pHEMT manufacturing," in *Proc. Int. Conf. Compd. Semicond. Manuf*, 2009.

[33] O. Yurduseven, "Wideband integrated lens antennas for terahertz deep space investigation," Ph. D. dissertation, Dept. Microelectron., Delft Univ. Technol., Delft, The Netherlands, 2016.

[34] J. van Rantwijk, M. Grim, and D. Van Loon, "Multiplexed readout for 1000 pixel arrays of microwave kinetic inductance detectors," *IEEE Trans. Microw. Theory Techn.*, vol. 64, no. 6, pp. 1876–1883, Jun. 2016.

[35] L. Bisigello, S. J. C. Yates, V. Murugesan, J. J. A. Baselmans, and A. M. Baryshev, "Calibration scheme for large kinetic inductance detector arrays based on readout frequency response," *J. Low Temp. Phys.*, vol. 184, no. 1, pp. 161–166, 2016. [Online]. Available: http://dx.doi.org/10.1007/s10909-016-1524-x

[36] J. J. A. Baselmans, S. J. C. Yates, P. Diener, and P. J. de Visser, "Ultra low background cryogenics test facility for far infrared radiation detectors," *J. Low Temp. Phys.*, vol. 167, pp. 360–366, 2012.

[37] P. J. De Visser, J. J. A. Baselmans, J. Bueno, N. Llombart, and T. M. Klapwijk, "Fluctuations in the electron system of a superconductor exposed to a photon flux," *Nat. Commun.*, vol. 5, p. 3130, 2014, doi:10.1038/ncoms4130.

[38] S. L. van Berkel, A. Garufo, N. Llombart, and A. Neto, "A quasi-analytical tool for the characterization of transmission lines at high frequencies [EM Programmer's Notebook]," *IEEE Antennas Propag. Mag.*, vol. 58, no. 3, pp. 82–90, Jun. 2016.

[39] D. Flanigan *et al.*, *Appl. Phys. Lett.*, vol. 108, pp. 10–15, 2016.

[40] T. Guruswamy, D. J. Goldie, and S. Withington, "Quasiparticle generation efficiency in superconducting thin films," *Supercond. Sci. Technol.*, vol. 27, 2014, Art. no. 55012.

[41] J. Zmuidzinas, "Superconducting microresonators: Physics and applications," *Ann. Rev. Condens. Matter Phys.*, vol. 3, pp. 169–214, 2012.

Lorenza Ferrari received the Ph.D. degree in applied physics from the University of Genoa, Genoa, Italy, in 2009, working on cryogenic detectors for astrophysics applications.

She then worked for one year at the INFN Genoa and Physikalisch–Technische Bundesanstalt Institute Berlin, Berlin, Germany, as a Postdoctoral Researcher on low temperature detectors for neutrino mass experiments. Since 2010, she has been working as an Instrument Scientist at SRON, Netherlands Institute for Space Research, Utrecht, The Netherlands. She is involved with SAFARI (SpicA FAR-infrared Instrument) and XIFU (X-ray Integral Field Unit spectrometer) experiments modeling and testing the focal plane assembly, as well as designing cryogenic facilities for performance validation of instruments components. Her current research interests include the development of microwave kinetic inductance detectors (MKIDs) for sub-mm applications and transition edge sensors (TESs) for far-IR frequency range focusing on optical characterization and application in scientific instruments.

Ozan Yurduseven (S'11) received the B.Sc. and M.Sc. (Hons.) degrees in electronics and communications engineering from Yildiz Technical University, Istanbul, Turkey, in 2009 and 2011, respectively, and the Ph.D. degree in electrical engineering from Delft University of Technology, Delft, The Netherlands, in 2016.

His Ph.D. degree research was on the development of dielectric lens antennas for THz space applications. During his Ph.D. degree, he spent six months as a Visiting Researcher in the Instituto de Telecomunicações, Instituto Superior Técnico, Lisbon, Portugal, working on the double shell dielectric lenses. He has authored or coauthored more than 30 publications in peer-reviewed journals and conferences. His current research interests include dielectric lens antenna for millimeter and sub-millimeter wave space applications, quasi-optical systems, numerical techniques in electromagnetics and metamaterials.

Dr. Yurduseven is a member of the IEEE Antennas and Propagation Society and the European Association on Antennas and Propagation. He was the recipient of the Best Student Paper Award at the European Conference on Antennas and Propagation in 2013. He is one of the coauthors of the conference proceeding that was awarded with the Best Paper on Electromagnetism and Antenna Theory of EuCAP 2016. He serves as a Reviewer for the IEEE TRANSACTION ON ANTENNAS AND PROPAGATION, IEEE ANTENNAS AND WIRELESS PROPAGATION LETTERS, and *IET Microwaves Antennas and Propagation*.

Nuria Llombart (S'06–M'07–SM'13) received the Master's degree in electrical engineering and Ph.D. degrees from the Polytechnic University of Valencia, Valencia, Spain, in 2002 and 2006, respectively.

During her Master's degree studies, she spent one year at the Friedrich-Alexander University of Erlangen-Nuremberg, Erlangen, Germany, and worked at the Fraunhofer Institute for Integrated Circuits, Erlangen, Germany. From 2002 to 2007, she was with the Antenna Group, TNO Defence, Security and Safety Institute, The Hague, The Netherlands, working as a Ph.D. student and afterwards as a Researcher. From 2007 to 2010, she was a Postdoctoral Fellow with the California Institute of Technology, working with the Submillimeter Wave Advance Technology Group, Jet Propulsion Laboratory, Pasadena, CA, USA. She was a Ramón y Cajal Fellow in the Optics Department, Complutense University of Madrid, Madrid, Spain, from 2010 to 2012. In September 2012, she joined the THz Sensing Group, Technical University of Delft, Delft, The Netherlands, where she is currently an Associate Professor. She has coauthored more than 150 journal and international conference contributions. Her research interests include the analysis and design of planar antennas, periodic structures, reflector antennas, lens antennas, and waveguide structures, with emphasis in the THz range.

Dr. Llombart was co-recipient of the H. A. Wheeler Award for the Best Applications Paper of 2008 in the IEEE TRANSACTIONS ON ANTENNAS AND PROPAGATION, the 2014 THz Science and Technology Best Paper Award of the IEEE Microwave Theory and Techniques Society, and several NASA awards. She was also the recipient of the 2014 IEEE Antenna and Propagation Society Lot Shafai Mid-Career Distinguished Achievement Award. She serves as a Board member of the IRMMW-THz International Society. In 2015, she was the recipient of European Research Council Starting Grant.

Stephen J. C. Yates received the Ph.D. degree from the University of Bristol, Bristol, U.K., in 2003, working on experimental low temperature techniques for condensed matter physics.

He then worked at the CNRS-CRTBT (now institute Nel) Grenoble, Grenoble, France, as a Postdoctoral Researcher on low temperature magnetism and superconductivity (2003–2004). He followed this also at CNRS-CRTBT with work on the development of low temperature detectors and techniques for astrophysics (2004–2006). He is currently an Instrument Scientist working on superconducting microwave kinetic inductance detectors at SRON, Netherlands Institute for Space Research, which he started in 2006. He has authored or coauthored more than 50 papers. His current research interests include MKID development for sub-mm applications, but also include a wider interest in device physics and superconductivity, optical design, and full end to end instrument characterization and performance.

Juan Bueno received the graduate degree in physics from the University of Cantabria, Santander, Spain, in 2003, and the Ph.D. degree from the University of Leiden, Leiden, The Netherlands, in 2007. During his Ph.D. degree, he studied quantum crystals at very low temperatures.

From 2007 to 2008, he was a Postdoctoral Fellow at the University of California at San Diego, La Jolla, CA, USA, continuing his work on quantum crystals. In 2008, he made the decision to switch research topics and interests from fundamental physics to the study of superconducting devices. He was awarded with a NASA Postdoctoral position (NPP), becoming a Post-Doctoral Researcher with the Jet Propulsion Laboratory, Pasadena, CA, USA, until 2010. During this time, he pioneered a new type of pair-breaking radiation detector, the quantum capacitance detector. After his time at JPL, he joined the Center for Astrobiology, Spain, in 2010 after receiving a JAE-doc grant, working mainly on kinetic inductance detectors (KIDs). He became an Instrument Scientist in 2012 at SRON—Netherlands Institute for Space Research, Utrecht, The Netherlands, working on the development of KIDs for sub-mm wave and far IR space-based observatories. He has authored or coauthored more than 30 peer-reviewed papers, a third of them as the lead author. His research interest concentrates on the development of ultra-sensitive broadband KIDs for future space-based missions.

Vignesh Murugesan received the M.Sc. degree in microsystem integration technology from the Chalmers University of Technology, Gothenburg, Sweden, in 2007.

He worked as a Process Integration Engineer from 2007 to 2008 for Infineon Technologies AG, Regensburg, Germany. From 2010 to 2013, he worked as a MEMS Process Engineer for Thermo Fisher Scientific, Enschede, The Netherlands. Since 2013, he has been working as a Process Engineer with the Microwave Kinetic Inductance Detectors Group, SRON Netherlands Institute for Space Research, Utrecht, The Netherlands. He is currently responsible for the fabrication and process development of MKID chips.

David J. Thoen was born in Nieuwveen, The Netherlands, in 1978. He received the B.S. degree in applied physics from the Fontys University of Technology, Eindhoven, The Netherlands, in 2008.

He started in 2007 as a Microwave Engineer with the Dutch Institute for Fundamental Energy Research (DIFFER, formerly known as the FOM Institute Rijnhuizen), Nieuwegein, The Netherlands, working on microwave diagnostics for real-time control of electron-cyclotron resonance heating of nuclear fusion plasmas in tokamaks. In 2010, he moved to the Cosmo Nanoscience Group, Delft University of Technology, Delft, The Netherlands, working on the development and fabrication of the Band 9 (600–720 GHz) superconductor/insulator/superconductor detector chips for the Atacama Large Millimeter Array. Since 2012, he has been working on microwave kinetic inductance detectors, from 2015, with the Terahertz Sensing Group, Delft University of Technology. He is responsible for the development and processing of MKID in the Kavli Cleanroom, Delft. He has coauthored more than 20 peer-reviewed papers. His research interests include reactive sputtering of niobium-titanium-nitride and quality control of thin films.

Akira Endo received the Ph.D. degree in astronomy (with "Prize for Encouragement in Research" analogous to *cum laude*) from the School of Science, University of Tokyo, Tokyo, Japan, in 2009. His dissertation was entitled "AIN Tunnel Barriers for Submillimeter Wave SIS Mixers."

Since 2009, he has been working as a Postdoctoral Researcher with the Kavli Institute of Nanoscience, Delft University of Technology, Delft, The Netherlands. From November 2014, he has been appointed as a Tenure Track Assistant Professor with the Department of Electrical Engineering, Faculty of Mathematics and Computer Science, Delft University of Technology. During 2011–2014, he conducted a combined NWO-Veni program and a JSPS postdoctoral research program "Probing the Cosmic History of Star Formation by Submillimeter Wave Ultrabroadband Spectroscopy using Superconducting Resonators." He is the co-PI of an NOW-M program "DESHIMA: On-chip Filterbank Spectrometer for Submillimeter Wave Cosmology," and he has recently been granted a NOW-Vidi program starting in 2014 entitled "Dawn of Superconducting Astrophotonics." These projects together aim at the development and demonstration of a superconducting on-chip filter bank spectrometer DESHIMA, which capitalizes on the collaborative development of MKIDs at the Delft University of Technology and SRON Netherlands Institute for Space Research.

Andrey M. Baryshev received the M.S. degree (summa cum laude) in physical quantum electronics from Moscow Physical Technical institute, Moscow, Russia, in 1993, and the Ph.D. degree in superconducting integrated receiver combining SIS mixer and flux flow oscillator into one chip from the Technical University of Delft, Delft, The Netherlands, in 2005.

He is currently an Associate Professor in Kapteyn Astronomical Institute, University of Groningen, Groningen, The Netherlands. He was previously a Senior Instrument Scientist with the SRON Low Energy Astrophysics Division, Groningen, The Netherlands, from 1998 to 2017. In 1993, he was an Instrument Scientist with the Institute of Radio Engineering and Electronics, Moscow, Russia, involved in the field of sensitive superconducting heterodyne detectors. In 2000, he joined an effort to develop an SIS receiver (600–720 GHz) for the Atacama Large Millimeter Array, where he designed the SIS mixer, quasi-optical system, and contributed to a system design. His current main research interests include application heterodybe and direct detectors for large focal plane arrays in THz frequencies and quasi-optical systems design and experimental verification.

Dr. Baryshev was the recipient of the NOW-VENI Grant for his research on heterodyne focal plan arrays technology in 2008 and, in 2009, he was the recipient of the EU commission Starting Researcher Grant for his research on focal plane arrays of direct detectors.

Jochem J. A. Baselmans was born in 1974. He received the Graduate degree and Ph.D. degree (*summa cum laude*) from the University of Groningen, Groningen, The Netherlands, in 1998 and 2002. His doctoral dissertation was entitled "Controllable Josephson Junctions."

He is currently a Senior Instrument Scientist with the SRON Netherlands Institute for Space Research, Utrecht, The Netherlands, where he has worked since 2002 with the Technology Division. Since 2015, he is also an Associate Professor with the THz Sensing Group, Delft University of Technology, Delft, The Netherlands. He started in 2002 as a Postdoctoral Instrument Scientist with the SRON Netherlands Institute for Space Research, Utrecht, The Netherlands, where he has worked until 2004 on hot electron bolometer mixers and very sensitive heterodyne radiation detectors for frequencies between 1 and 5 THz. In 2005, he moved to SRON Utrecht, and started working on microwave kinetic inductance detectors, after a three month visit to the California Institute of Technology, Pasadena, CA, USA. He has authored or co-authored over 100 papers.

Dr. Baselmans was the recipient of an ERC Consolidator Grant to develop an advanced imaging spectrometer based upon MKIDs in 2015. He currently leads the Dutch effort on the development of microwave kinetic inductance detectors.